Investigation of supersonic heat-conductivity hyperbolic waves in radiative ablation flows

G. Varillon [1,2,*] J.-M. Clarisse,[1] and A. Couairon [2]

[1]*CEA, DAM, DIF, F-91297 Arpajon, France*
[2]*CPHT, CNRS, École Polytechnique, Institut Polytechnique de Paris, F-91128 Palaiseau, France*

We carry out a numerical investigation of three-dimensional linear perturbations in a self-similar ablation wave in slab symmetry, representative of the shock transit phase of a pellet implosion in inertial confinement fusion (ICF). The physics of ablation is modeled by the equation of gas dynamics with a nonlinear heat conduction as an approximation for radiation transport. Linear perturbation responses of the flow, its external surface, and shock-wave front, when excited by external pressure or heat-flux perturbation pulses, are computed by fully taking into account the flow compressibility, nonuniformity, and unsteadiness. These responses show the effective propagation, at supersonic speeds, of perturbations from the flow external surface through the whole conduction region of the ablation wave, beyond its Chapman-Jouguet point, and up to the ablation front, *after* the birth of the ablation wave. This supersonic forward propagation of perturbations is evidenced by means of a set of appropriate pseudocharacteristic variables and is analyzed to be associated to the "heat-conductivity" waves previously identified by Clarisse *et al.* [J. Fluid Mech. **848**, 219 (2018)]. Such heat-conductivity linear waves are found to prevail over heat diffusion as a feedthrough mechanism [Aglitskiy *et al.*, Philos. Trans. R. Soc. A **368**, 1739 (2010)] for perturbations of longitudinal characteristic lengths of the order of—or larger than—the conduction region size, and long transverse wavelengths with respect to this region size, and over time scales shorter to much shorter than the shock transit phase duration. This mechanism, which results from the dependency of the heat conductivity on temperature and density in conjunction with a flow temperature stratification, is expected to occur for other types of nonlinear heat conductions—e.g., electron heat conduction— as well as to be efficient at transmitting large scale perturbations from the surrounding of an ICF pellet to its inner compressed core at later times of its implosion. Besides, the proposed set of pseudocharacteristic variables are recommended for analyzing perturbation dynamics in an ablation flow as it furnishes additional propagation information over the fundamental linear modes of fluid dynamics [Kovásznay, J. Aeronautic. Sci. **20**, 657 (1953)], especially in the flow conduction region.

I. INTRODUCTION

The hydrodynamic stability of radiation-driven ablation flows is a key issue in inertial confinement fusion (ICF) where a sufficiently symmetric implosion of a spherical pellet is expected to achieve thermonuclear burn. Such flows, which originate from exposing the outer shell of a pellet to a growing incident heat flux, present the radial structure of an inward-propagating deflagration, or ablation, wave where a shock front precedes a subsonic heat front that coincides with the leading edge of the heated material expansion wave [1,2]. Inherently unsteady, these flows are compressible, strongly accelerated, and highly nonuniform with a steep heat front, owing to the strong nonlinearity of the heat transport and the intense incident heating.

At the early stage of an ICF implosion, a forerunning converging shock wave compresses and sets into an inward motion the outer pellet shell—the ablator—until it breaks out at the ablator inner surface, during the so-called shock transit phase. This shock front is followed by an ablation layer which sets the compressed medium in expansion, resulting in an inward thrusting force that implodes the shell. Hydrodynamic instabilities emerging during the shock transit phase will seed the subsequent acceleration phase with perturbations. Many works have shown that perturbations strongly develop during the acceleration stage, resulting in the loss of symmetry of the implosion and eventually inhibiting ignition of fusion reactions (see [3] and references therein). The understanding of hydrodynamic perturbation dynamics during the shock transit phase is therefore of primary importance to ICF.

These perturbation dynamics have been classically analyzed according to two distinct perturbed flows. One corresponds to the ablation by a perturbed incoming heat flux— or illumination asymmetries—of an otherwise unperturbed medium at rest. When the external heat source is a laser light—laser-driven ablation—the flow perturbation mechanisms at stake have been designated by the term laser imprinting [4]. The other configuration consists in the ablation, by a uniform heat flux, of a uniform medium at rest presenting an initially rippled external surface. The resulting perturbation dynamics, due to the configuration resemblance with that of the Richtmyer-Meshkov instability [5,6], has been termed ablative Richtmyer-Meshkov instability [7]. In both cases the

---
*gregoire.varillon@polytechnique.edu

corresponding ablation waves are perturbed over their whole finite spatial extent—i.e., from the fluid external surface up to the forerunning shock front—and this right from their onset.

Theoretical investigations of these perturbation configurations have exclusively considered laser-driven ablation and have relied mostly on the standard assumptions in practice for the modeling of ICF ablation flows and of their instabilities, namely stationary quasi-isobaric ablation and, in certain instances, discontinuous ablation fronts (e.g., Ref. [8]). These investigations along with numerical simulations and dedicated experiments have lead to the conclusion that ablation-front deformations of transverse wavelengths smaller than the thickness, say l_{cond}, of the flow region where heat conduction dominates over advection—conduction region—undergo damped oscillations, whereas perturbations of wavelengths much larger than l_{cond} may grow as a result of the ablative Richtmyer-Meshkov instability and, possibly, Darrieus-Landau instability mechanisms [4,7,9–17]. A weak acceleration of the ablation front and consequently the dominant influences of the restoring force due to the ablation "rocket effect" and of the damping provided by mass ablation, in conjunction with the perturbations left behind the oscillating perturbed shock front, are responsible for this damped oscillatory regime. For sufficiently long wavelengths, deformation growth has been found to be roughly linear in time rather than exponential, although, according to theory, exponential growth could occur, under certain conditions, due to the Darrieus-Landau instability [7,12,15–17]. The confinement of the flow by the forerunning shock front and the surface of energy deposition is even more influential in this regime.

Due to the multiplicity of phenomena at stake in ablation waves, the standard modeling of radiation-driven ablation in ICF has relied on simplifying assumptions: i.e., an isothermal expansion, a stationary ablation region, and in certain cases an isobaric approximation for this region [1,18]. Nowadays, ICF ablation flows are routinely studied by means of multiple-physics simulations which are however computationally more demanding [3].

An intermediate approach between simplified modelings and simulations uses self-similar solutions to the Euler equations with nonlinear heat conduction [19–21]. Such solutions, known since Marshak [22], present the advantage over isobaric, isothermal, or stationary solutions of rendering, without further approximations, compressibility, nonuniformity, and unsteadiness of ablation waves. They have been exploited to model ICF-type ablation flows [23–25]. Indeed these self-similar flows present the essential characteristics of an ablation wave as illustrated on Fig. 1(a): (i) a leading shock front, (ii) a quasi-isentropic compression (postshock) region, (iii) an ablation layer, and (iv) an expansion wave where heat conduction dominates (the conduction region). In addition, these self-similar solutions have been used for the computation of linear perturbation responses of ablation waves for configurations of illumination asymmetries and of the ablative Richtmyer-Meshkov instability [19–21,26]. In addition to the two identified regimes of perturbation growth and damped oscillations for transverse wavelengths, respectively, larger and smaller than the conduction region thickness, these results have pointed out the determining influence of the
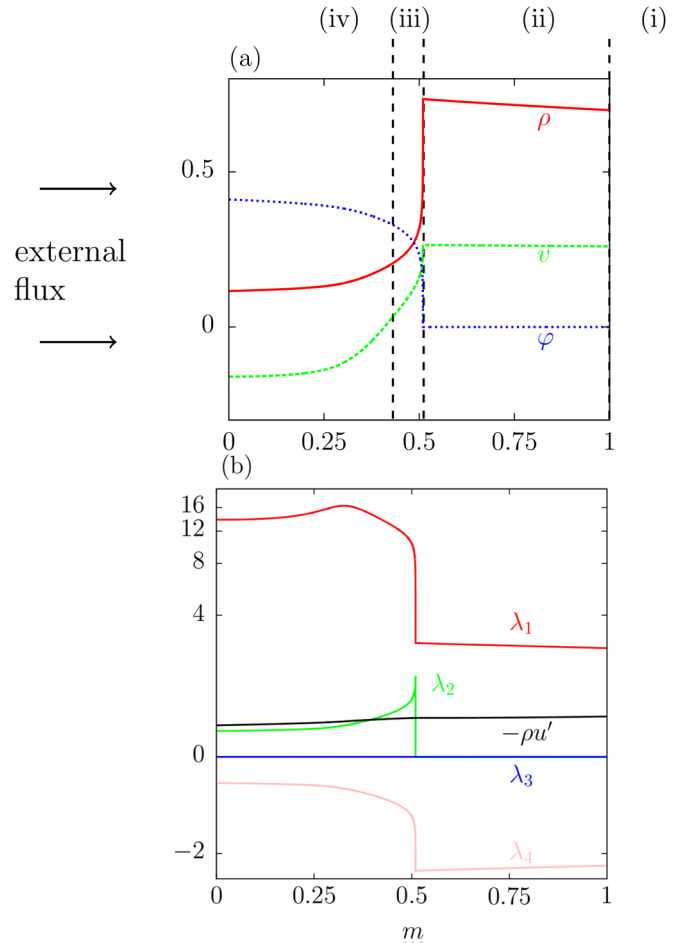

FIG. 1. (a) Base flow profiles in the Lagrangian coordinate m scaled by the function defined by $\mathrm{slog}_1(\cdot) \equiv \mathrm{sgn}(\cdot)\log(1+|\cdot|)$. Density ($\rho$), longitudinal velocity (v), and heat flux (φ). (b) Characteristic wave speeds [Eq. (9)] ($\lambda_{1,2,3,4}$) and fluid momentum relative to the ablation front ($-\rho u'$).

mean flow unsteadiness on perturbation dynamics at long to moderate wavelengths, including the transition between the two regimes. In particular, for the case of illumination asymmetries, perturbation growth at long wavelengths turns out to be dominated by the mean flow stretching and consequently to be algebraic in time.

In the present work, we aim at gaining insight into the setting up of perturbations in an already existing and unperturbed ablation wave, as a result of a perturbation excitation at the flow external surface. In that respect, this configuration differs from those of illumination asymmetries and ablative Richtmyer-Meshkov instability with the consequences that perturbations will here present short-term dynamics that are absent from such configurations. We analyze the responses of the state variables along with the deformations of the external surface, ablation front, and shock front, with the aim of identifying essential physical mechanisms that rule perturbation transmission across the flow. This work goes beyond what was done in Ref. [21], with respect to wave propagation and the analysis of the flow conduction region. Indeed, a local analysis of ablation waves in terms of linear waves propagating in the longitudinal direction reveals

that temperature and density stratification in the conduction region, in conjunction with the heat-conductivity nonlinearity, lead to the existence of a family of supersonic forward-propagating waves in this region [25]. Classical description of ablation waves, because of the isothermal assumption, are unable to render such phenomenon, hence the interest of self-similar solutions. Here we extend the analysis of Ref. [25] by considering and numerically solving the exact system of evolution equations for three-dimensional linear perturbations about self-similar ablation waves [19,20]. The entire deflagration structure of a nonuniform and unsteady ablation wave is described, smoothly, from the fluid external surface where an incoming radiation flux and an external pressure are applied, up to the forerunning shock front. The ablation flow is considered in slab symmetry which is a reasonable approximation insofar as the shock transit phase corresponds to the beginning of a target implosion: curvature effects and convergence effects are actually negligible for sufficiently small perturbation transverse wavelengths. Besides, these solutions assume that the fluid is optically thick, which is an approximation for actual ICF target ablation. We focus on a self-similar ablation flow with a fast expansion of its conduction region (i.e., presenting an isothermal Chapman-Jouguet point) as it presents the main characteristics of the shock transit phase of an ICF pellet implosion [25].

We first (Sec. II) present our model and characterize the chosen ablation flow. Evolution equations are introduced for three-dimensional linear perturbations. The framework of our pseudocharacteristic analysis is presented (Sec. III). Results (Sec. IV) show that the pseudocharacteristic analysis is suitable for understanding the evolution of perturbations. Section IV B presents an important result of this work: we assess quantitatively the ability of supersonic heat-conductivity linear waves to propagate from the external surface beyond the Chapman-Jouguet point. This effect is shown to be due to an advection mechanism which may propagate not only temperature fluctuations, as heat diffusion does, but also density and velocity fluctuations. The efficiency of this propagation is quantified depending on heat diffusion intensity, as well as its impact on ablation front and shock front deformations. Approximate evolution equations are identified in the case of advection dominated and diffusion dominated flow perturbations; couplings in the ablation front layer are then described. In Sec. VI we discuss the implications of our results for analyzing perturbation evolution in actual ICF target implosions.

II. MODEL

In order to investigate the deflagration structure of a nonuniform and unsteady ablation flow, we will consider the evolution of three dimensional linear perturbations of a self-similar ablation flow which exhibits a fast expansion of its conduction region, a situation typical of the shock transit phase of an ICF pellet implosion [18,23].

A. Governing equations

We consider the motion of a polytropic gas in a semi-infinite slab subject to an irradiation flux and material pressure at its external boundary. The external irradiation flux is sufficiently high so that radiation heat conduction dominates any other diffusive effect (e.g., viscosity). However, the fluid temperature is sufficiently low for radiation pressure and radiation energy to be negligible compared to material pressure and internal energy. The material is considered at local thermodynamic equilibrium, allowing us to use a fluid model to describe its motion. Assuming that this motion is along the x direction of a Cartesian system of coordinates (O, x, y, z), the equations of motion are written, in dimensionless form and in the Lagrangian coordinate m, where $dm = \rho\, dx$, as

$$\partial_t(1/\rho) - \partial_m v = 0,$$
$$\partial_t v + \partial_m p = 0,$$
$$\partial_t(e + v^2/2) + \partial_m(pv + \varphi) = 0, \qquad (1)$$

where ρ, v, p, and e denote, respectively, the fluid density, velocity, pressure, and specific internal energy, and the heat flux φ is related to the fluid density and temperature T through the expression [24]

$$\varphi = -\rho^{-\mu} T^{\nu} \rho\, \partial_m T \equiv \Psi(\rho, T, \partial_x T), \quad \mu \geqslant 0, \ \nu > 1. \quad (2)$$

This system is closed by the dimensionless equation of state

$$p = \rho T, \quad e = \frac{T}{\gamma - 1},$$

with γ the adiabatic gas exponent. Self-similar reductions of Eq. (1) arise if the time dependence of the incident heat flux and pressure at the external surface follow specific power laws, namely

$$\varphi(0, t) = \mathcal{B}_\phi t^{3\alpha - 3}, \quad p(0, t) = \mathcal{B}_p t^{2\alpha - 2}, \quad \text{for } t > 0,$$
$$\text{with } \alpha = \frac{2\nu - 1}{2\nu - 2}, \qquad (3)$$

and for an initial state given by $(\rho, v, T) = (1, 0, 0)$ for $m \geqslant 0$ [19,22]. For certain values of the boundary parameters $(\mathcal{B}_p, \mathcal{B}_\varphi)$, such solutions present the features of an ablation wave extending from the flow external surface $(m = 0)$ through an ablation front up to the forerunning isothermal shock front [24,25]. This shock front is preceded by an infinitesimal radiation wavelet penetrating the cold fluid [22]. When values of the heat-flux parameter $\mathcal{B}_\phi$ are not too high, this wavelet is negligible and may be combined with the isothermal shock front into a nonisothermal shock front [22,24,25]. Solutions to Eq. (1) describe smoothly all features of a radiative ablation wave without any further approximation and notably account for the temperature and density stratification of the conduction region. In the present case, highly accurate solutions to Eqs. (1)–(3) are obtained by means of an adaptive multidomain Chebyshev spectral method [27].

In the present work we consider the case of a self-similar ablative wave driven by a sufficiently low external pressure $(\mathcal{B}_\phi, \mathcal{B}_p) = (0.8, 0.31)$ with Kramers' fully ionized gas model for radiation conduction $(\mu = 2, \nu = 13/2)$ [2,25]. This ablation flow presents the essential features of the shock transit phase of an ICF implosion, namely, a supersonic expansion velocity relative to the ablation front, and a relatively high ratio of convective to inertial effects—Froude number—at the ablation front (Table I).

TABLE I. Characteristic hydrodynamic numbers of the base flow (defined in [25]): Ma is the Mach number and Fr the Froude number relative to the ablation front, completed by the reduced length L_{cond} of the conduction region and the ratio of the minimum of the temperature gradient reduced length L_T to the flow total reduced length L_{tot}.

max Ma	1.045
Ma$|_{\text{af}}$	0.22
Fr$|_{\text{af}}$	80.3
L_{cond}	1.29
L_T/L_{tot}	3.00×10^{-5}

As a consequence of the self-similarity, lengths evolve as $l(t) = t^{\alpha}L$, where L denotes reduced length functions. The conduction region of length $l_{\text{cond}}(t)$ is the region between the external surface ($m = 0$) and the ablation front (af), which is defined as the location of the minimum of the temperature gradient length. This minimum gradient length defines the characteristic thickness of the ablation front $l_T(t)$. The ratio $l_T(t)/l_{\text{tot}}(t)$, where $l_{\text{tot}}(t)$ is the flow total length—i.e., the distance between the external surface and the shock wave front—characterizes the stiffness of the flow (Table I).

B. Linear perturbations

Three-dimensional linear perturbations of the above self-similar ablative waves are considered using a Eulerian description in the coordinate system (m, y, z). The resulting system of partial differential equations in physical space is replaced by a one-dimensional system in the yz-Fourier space. With the notation $\widehat{f}$ for the linear perturbation yz-Fourier component of the base flow quantity f with transverse wave number $k_{\perp} = \sqrt{k_y^2 + k_z^2}$, this system reads

$$\partial_t \widehat{\mathbf{U}} = L\widehat{\mathbf{U}} \equiv -\mathbf{A}\partial_{m^2}^2\widehat{\mathbf{U}} - \mathbf{B}\partial_m\widehat{\mathbf{U}} - \mathbf{C}\widehat{\mathbf{U}}, \quad (4)$$

with $\widehat{\mathbf{U}} = [\widehat{\rho}\ \widehat{v}\ \widehat{d}_{\perp}\ \widehat{T}]^{\top}$, where $\widehat{d}_{\perp}$ denotes the Fourier component of the transverse divergence of the transverse velocity, and with the matrices $\mathbf{A}$, $\mathbf{B}$, and $\mathbf{C}$ defined by

$$\mathbf{A} = \begin{pmatrix} 0 & 0 & 0 & 0 \\ 0 & 0 & 0 & 0 \\ 0 & 0 & 0 & 0 \\ 0 & 0 & 0 & C_v^{-1}\rho\Psi_{T'} \end{pmatrix},$$

$$\mathbf{B} = \begin{pmatrix} 0 & \rho^2 & 0 & 0 \\ T & 0 & 0 & \rho \\ 0 & 0 & 0 & 0 \\ C_v^{-1}\Psi_{\rho} & C_v^{-1}p & 0 & \mathsf{B}_{44} \end{pmatrix},$$

$$\mathbf{C} = \begin{pmatrix} \rho\partial_m v & \rho\partial_m\rho & \rho & 0 \\ T\partial_m\rho/\rho & \rho\partial_m v & 0 & \rho\partial_m T \\ k_{\perp}^2 T/\rho & 0 & 0 & -k_{\perp}^2 \\ \mathsf{C}_{41} & \rho\partial_m T & C_v^{-1}T & \mathsf{C}_{44} \end{pmatrix},$$

$$\mathsf{B}_{44} = C_v^{-1}[\partial_m(\rho\Psi_{T'}) + \Psi_T],$$

$$\mathsf{C}_{41} = C_v^{-1}(\partial_m\Psi_{\rho} - \rho^{-1}\partial_m\varphi),$$

$$\mathsf{C}_{44} = C_v^{-1}[\rho\partial_m v + \partial_m\Psi_T - k_{\perp}^2\rho^{-1}\Psi_{T'}].$$

The longitudinal perturbation of the heat flux expands as $\widehat{\varphi}_x = \widehat{\rho}\,\Psi_{\rho} + \widehat{T}\,\Psi_T + \rho\Psi_{T'}\partial_m\widehat{T}$, where Ψ_{ρ}, Ψ_T, and $\Psi_{T'}$ stand for the partial derivatives of Ψ [Eq. (2)] with respect to the density, the temperature, and the temperature gradient. Similarly, the transverse perturbation of the heat flux expands as $\nabla_{\perp} \cdot \widehat{\boldsymbol{\varphi}}_{\perp} = k_{\perp}^2\Psi_{T'}\widehat{T}$.

The external surface and shock front are also perturbed and their linear deformations are denoted $\widehat{X}_{\text{es}}(t)$ and $\widehat{X}_{\text{sf}}(t)$, respectively. Perturbed boundary conditions arise from a first order expansion of Eq. (3) between the mean position of the boundary surface and its perturbed position [20]. At the external surface, perturbations in pressure and heat flux are imposed:

$$\widehat{p}_{\text{es}}(t) = \widehat{p}(0, t) + \widehat{X}_{\text{es}}(t)\rho(0, t)\partial_m p|_{m=0}, \quad (5a)$$

$$\widehat{\varphi}_{\text{es}}(t) = \widehat{\varphi}(0, t) + \widehat{X}_{\text{es}}(t)\rho(0, t)\partial_m\varphi|_{m=0}, \quad (5b)$$

and the following kinematic relation at this material surface applies:

$$\widehat{v}_{\text{es}}(t) = \dot{\widehat{X}}_{\text{es}}(t) = v(0, t) + \widehat{X}_{\text{es}}(t)\rho(0, t)\partial_m v|_{m=0}. \quad (5c)$$

At the shock front, Rankine-Hugoniot (RH) relations are perturbed to first order and take the form of four linear equations relating flow perturbations downstream to the shock front, $\widehat{\mathbf{U}}_{\text{sf}-}$, to shock front deformation, $\widehat{X}_{\text{sf}}$, shock front deformation velocity, $\dot{\widehat{X}}_{\text{sf}}$, and to the upstream state perturbation $\widehat{\mathbf{U}}_{\text{sf}+}$, say

$$R_{\text{RH}}(\widehat{\mathbf{U}}_{\text{sf}-}, \widehat{X}_{\text{sf}}, \dot{\widehat{X}}_{\text{sf}}, \widehat{\mathbf{U}}_{\text{sf}+}) = \mathbf{0}. \quad (6)$$

III. LOCAL CHARACTERISTIC ANALYSIS

Flow perturbations $\widehat{\mathbf{U}}$ are expressed in a new basis constructed by retaining the sole advection term in Eq. (4). The corresponding first-order system is written as

$$\mathbf{R}^{-1}\partial_t\widehat{\mathbf{U}} + \mathbf{\Lambda}(m, t)\mathbf{R}^{-1}\partial_m\widehat{\mathbf{U}} = \mathbf{0}, \quad (7)$$

where

$$\mathbf{\Lambda} = \text{diag}(\lambda_i) = \mathbf{R}^{-1}\mathbf{B}\mathbf{R}, \quad (8)$$

with $\mathbf{R}$ the matrix of local right eigenvectors of $\mathbf{B}(m, t)$. The eigenspectrum of $\mathbf{B}$ comprises the null eigenvalue, say $\lambda_3 = 0$, with associated normalized eigenvector given by $\mathbf{R}_3 = [0\,0\,1\,0]^{\top}$. The remaining eigenvalues, which are determined numerically, turn out to be all real and distinct—say $\lambda_1 > \lambda_2 > \lambda_4$ with $\lambda_4 < 0$—at any flow location m and time t, thus granting the hyperbolic property to system [Eq. (7)]. At any point (m, t), this system defines local characteristics as

$$(\mathbf{R}^{-1})_{ij}d\widehat{\mathbf{U}}_j = 0 \quad \text{along } \mathcal{C}_i : dm/dt = \lambda_i(m, t), \quad (9)$$

for $i = 1 \ldots 4$. Eigenvalues and eigenvectors of $\mathbf{B}$ are computed numerically [Fig. 1(b)] and the identification of the corresponding characteristics as families of propagating waves is given in Table II. In the conduction region, sufficiently far from the ablation layer, the characteristics $\mathcal{C}_2$ ($\mathcal{C}_4$) amount

TABLE II. Identification of the characteristic waves [Eq. (7)] in the conduction region and the postshock region (adapted from Table 6 in [25]).

	Conduction region	Postshock region
$\mathcal{C}_1$	Heat conductivity	Forward quasi-isentropic acoustic
$\mathcal{C}_2$	Forward quasi-isothermal acoustic	Quasientropy
$\mathcal{C}_3$	Transverse velocity	Transverse velocity
$\mathcal{C}_4$	Backward quasi-isothermal acoustic	Backward quasi-isentropic acoustic

to quasi-isothermal acoustic waves propagating in the forward (respectively backward) direction of the flow, while the characteristics $\mathcal{C}_1$ correspond to supersonic forward-propagating waves which advect fluctuations of heat-flux perturbations [25]. These "heat conductivity" waves are ruled by the dependence of the heat-flux function Ψ [Eq. (2)] on density and temperature [25]. While crossing the ablation front from the conduction region to the postshock region, heat conductivity waves $\mathcal{C}_1$ are converted into quasi-isentropic forward acoustic waves, forward quasi-isothermal acoustic waves are transformed into quasi-entropy waves $\mathcal{C}_2$, and backward quasi-isothermal acoustic waves $\mathcal{C}_4$ are similarly converted into quasi-isentropic acoustic waves. The characteristics $\mathcal{C}_3$ represent the advection, at the base flow fluid velocity, of transverse dilatation motions of the fluid, and this regardless of the flow location. The expansion of the conduction region in the present flow [Fig. 1(a)] is sufficiently strong for the fluid velocity relative to the ablation front to exceed the local sound speed, thus defining a Chapman-Jouguet (CJ) point: cf. the intersection point, for $m < 0.5$, between the curves for λ_2 and $-\rho u'$ in Fig. 1(b). Acoustic perturbations existing further downstream this CJ point cannot trace back the expansion flow, cross the CJ point, and reach the ablation layer. On the contrary, heat conductivity waves propagate beyond this CJ point although the expansion velocity is supersonic, because this wave speed exceeds the expansion velocity (λ_1 on Fig. 1). Within the postshock region, and at a sufficient distance away from the ablation layer, characteristics $\mathcal{C}_1$ and $\mathcal{C}_4$ come down to quasi-isentropic acoustic waves propagating, respectively, in the forward and backward directions, while characteristics $\mathcal{C}_2$ reduce to quasientropy waves moving approximately at the base flow velocity.

System Eq. (4) is then expressed in the pseudocharacteristic variables $\widehat{\mathcal{W}} = \mathbf{R}^{-1}\widehat{\mathbf{U}}$ as

$$\partial_t \widehat{\mathcal{W}} + \mathcal{A}\partial_{m^2}^2 \widehat{\mathcal{W}} + \mathbf{\Lambda}\partial_m \widehat{\mathcal{W}} + \mathcal{C}\widehat{\mathcal{W}} + \mathbf{\Delta}\widehat{\mathcal{W}} = \mathbf{0}, \quad (10a)$$

where

$$\mathcal{A} = \mathbf{R}^{-1}\mathbf{A}\mathbf{R}, \quad \mathcal{C} = \mathbf{R}^{-1}\mathbf{C}\mathbf{R}, \quad (10b)$$

and

$$\mathbf{\Delta}\widehat{\mathcal{W}} = \mathbf{R}^{-1}[\partial_t \mathbf{R} + \mathbf{A}(\partial_{m^2}^2 \mathbf{R}) + \mathbf{B}(\partial_m \mathbf{R})]\widehat{\mathcal{W}} + 2\mathbf{R}^{-1}\mathbf{A}\partial_m \mathbf{R}\partial_m \widehat{\mathcal{W}}$$
$$= \mathbf{\Delta}_0\widehat{\mathcal{W}} + \mathbf{\Delta}_1\partial_m \widehat{\mathcal{W}}. \quad (10c)$$

In this formulation, the diffusion coefficients of the pseudocharacteristic variables $\widehat{\mathcal{W}}_i$ are given by the diagonal elements $\mathcal{A}_{ii}$ of $\mathcal{A}$ while off-diagonal elements determine the coupling between these different variables through their second-order derivatives or second derivative coupling. The amplification matrix $\mathcal{C}$ contains both actual (self-

)amplification coefficients—the diagonal elements $\mathcal{C}_{ii}$—and amplitude coupling coefficients—the off-diagonal elements. Advection terms are decoupled by construction. The matrix $\mathbf{\Delta}$ gathers terms originating from time and space dependencies of eigenvectors. Setting $\mathbf{\Delta} = \mathbf{0}$ into Eq. (10a) corresponds to a local decomposition of Eq. (4) in the characteristic basis of Eq. (7), which holds at any point (m, t) but which does not constitute an evolution equation for $\widehat{\mathcal{W}}$ as Eq. (10a) is no longer equivalent to Eq. (4).

IV. RESPONSES TO EXTERNAL PERTURBATIONS

We now investigate how linear perturbations of Eq. (1) propagate, with the help of the pseudocharacteristic basis constructed in Sec. III. Numerical solutions to the system Eqs. (4)–(6) are computed, in the Lagrangian variable m, using the same multidomain pseudospectral method as for the base flow and, in time, with a three-step implicit-explicit Runge-Kutta scheme. Boundary conditions are handled using a penalty method, while matching conditions at subdomain interfaces are enforced exactly. The numerical code performs computations over each subdomain in parallel using the MPI paradigm with a single process per subdomain. Starting from a zero perturbation initial state ($t_0 = 1$), the system is perturbed at the external surface with a heat flux or pressure pulse given by

$$\widehat{\varphi}_{\text{es}}(t) = \varphi(0, t) \sin^4(\omega_1[t - t_0]),$$

with

$$\omega_1 = \frac{2\pi \lambda_1(m = 0, t_0)}{n \rho \, l_{\text{cond}}(t_0)}, \quad (11a)$$

or

$$\widehat{p}_{\text{es}}(t) = p(0, t) \sin^4(\omega_2[t - t_0]),$$

with

$$\omega_2 = \frac{2\pi \lambda_2(m = 0, t_0)}{n \rho \, l_{\text{cond}}(t_0)}, \quad (11b)$$

for $t_0 \leqslant t \leqslant t_0 + \pi/\omega_i$ or zero otherwise. The durations of these pulses correspond approximately to the time needed for the corresponding wave ($\mathcal{C}_1$ or $\mathcal{C}_2$) to travel n times the length of the conduction region. The power four on the sine functions ensures a smooth transition at t_0 and $t_0 + \pi/\omega_i$.

Solutions to Eq. (4) are projected on pseudocharacteristic variables $\widehat{\mathcal{W}}_i$ defined in Eq. (7). The various quantities are presented in (m, t) diagrams in which fluid particles move at constant m. On Figs. 2–5, 7, and 10, the mean position of the external surface is $m = 0$ by definition. Similarly, the mean position of the ablation layer (the shock front) is labeled
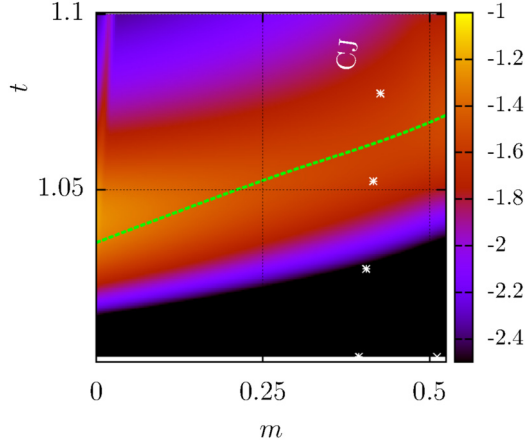
FIG. 2. Projection of the solution to Eq. (4) for a heat-flux perturbation $(n, k_\perp) = (4, 1)$ on pseudocharacteristic $\widehat{\mathcal{W}}_1$ in the conduction region in logscale. The dashed line represents a $\mathcal{C}_1$ characteristic originating from the pulse half height [Eq. (11)]. Trajectory of the CJ point (∗) is also indicated.

"af" ("sf"). The position of the CJ point is labeled "CJ." The cold fluid at rest $[m > m_{sf}(t)]$ is free from any source of perturbation. For visualization purposes we define the function $\text{slog}_a(x) = \text{sgn}(x) \log(1 + a|x|)$ for any real number x and positive parameter a. In addition, colored dashed lines in (m, t) diagrams represent exact characteristic trajectories defined in Eq. (9) originating from pulse half-heights [Eq. (11)] at the external surface or from other remarkable points.

Responses to Eq. (4) for an external perturbation tend to propagate close to linear hyperbolic waves. When perturbed with a heat-flux pulse $(n, k_\perp) = (4, 1)$, the signal follows, qualitatively, a $\mathcal{C}_1$ characteristic originating from the half height of the heat-flux pulse perturbation at the external surface (Fig. 2). The projection of the same solution on the pseudocharacteristic variable $\widehat{\mathcal{W}}_2$ shows no propagation beyond the CJ point [Fig. 4(b)]. In terms of primitive variables (Fig. 3), the only significant signal propagating through the conduction region is a temperature perturbation. This is coherent with the components of $\widehat{\mathcal{W}}_1$ in the basis of primitive variables (Fig. 11).

An external pressure perturbation [Fig. 5(b)] leads to a spread $\widehat{\mathcal{W}}_1$ signal propagating in the conduction region [Fig. 5(a)]. Such a perturbation follows a $\mathcal{C}_1$ characteristic originating from the half height of the pressure perturbation pulse at the external surface.

An external heat-flux perturbation is primarily converted into a heat-conductivity wave perturbation $\widehat{\mathcal{W}}_1$ [Fig. 4(a)], while an external pressure perturbation is primarily converted into a forward quasi-isothermal perturbation $\widehat{\mathcal{W}}_2$ [Fig. 5(b)]. We observe a posteriori that response of Eq. (4) to a heat flux or a pressure perturbation follows *a priori* characteristic trajectories $\mathcal{C}_i$ [Eq. (7)], either on the projection on pseudocharacteristic variables (Figs. 4 and 5) or on primitive variables (Fig. 3). The heat-conductivity wave signal $(\widehat{\mathcal{W}}_1)$ is the only one able to trace back the expansion flow beyond the CJ point. The heat-flux perturbation then interacts with the ablation layer where high gradients induce couplings with a reflected backward quasi-isothermal backward acoustic signal
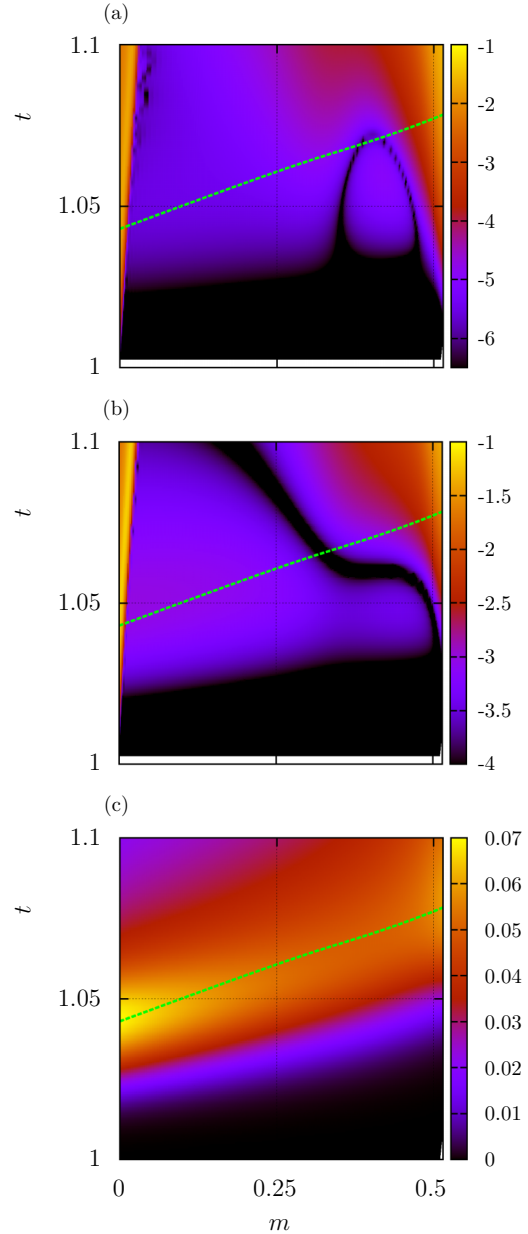

FIG. 3. Perturbation in (a) density in logscale, (b) longitudinal velocity in logscale, and (c) temperature in slog_1 scale, for a heat-flux perturbation with $(n, k_\perp) = (4, 0)$. The dashed line represents a $\mathcal{C}_1$ characteristic originating from the pulse half height [Eq. (11)].

$(\widehat{\mathcal{W}}_4)$ in the conduction region, and a forward quasi-isentropic acoustic signal $(\widehat{\mathcal{W}}_1)$ transmitted to the postshock region. We observe the formation of a system of reflected traveling waves in the postshock region, composed of quasi-isothermal acoustic waves and quasi-isentropic waves: see Fig. 6 for a schematic representation. Such reflected waves are unlikely to appear in the conduction region because, at the external surface, backward quasi-isothermal acoustic waves are mostly reflected into forward quasi-isothermal acoustic waves unable to propagate beyond the CJ point.

As mentioned above, while crossing the ablation layer, a perturbation $\widehat{\mathcal{W}}_1$ is partly reflected into the conduction region and partly transmitted to the postshock region, but a third
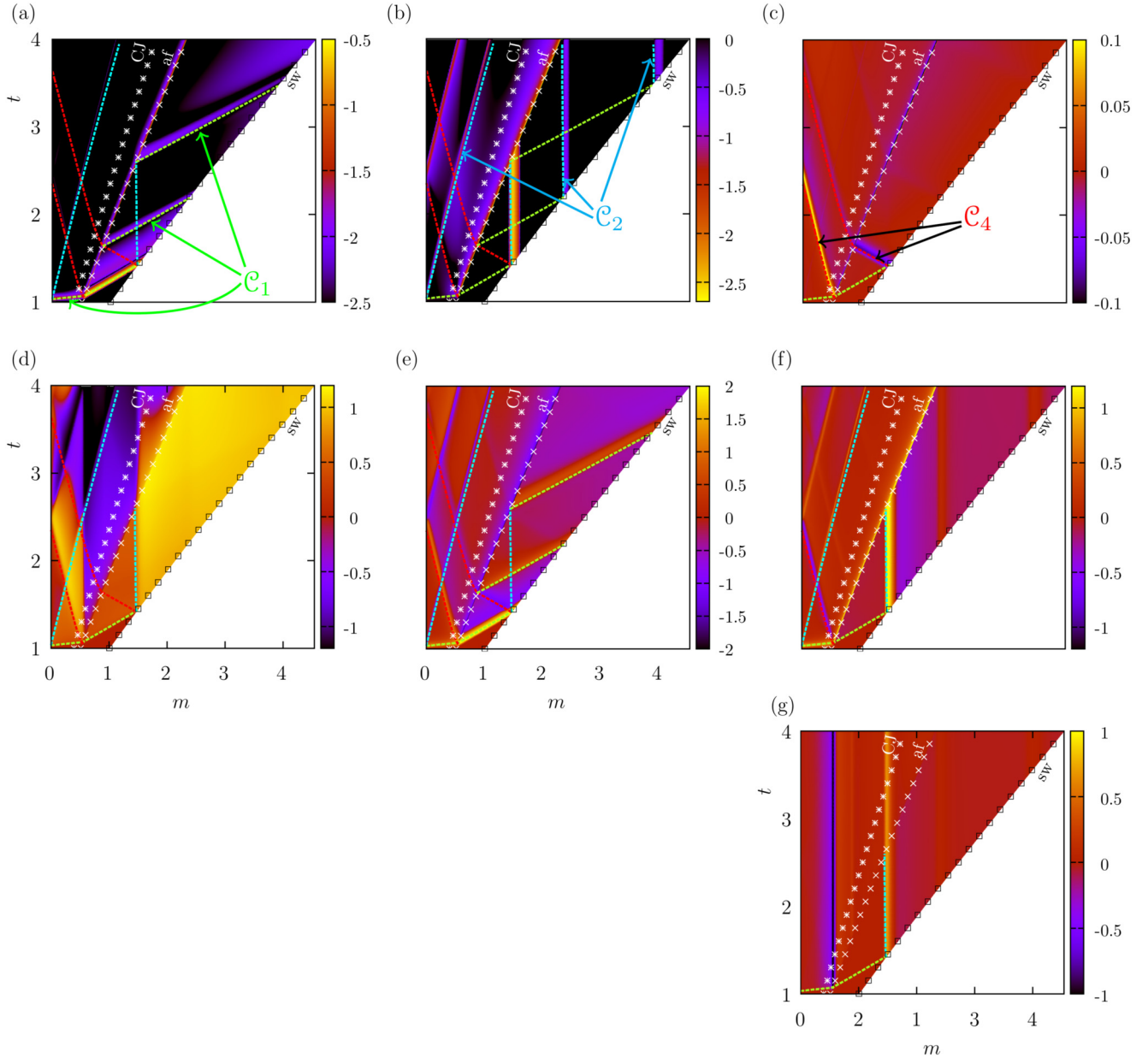
FIG. 4. Response of Eq. (4) to a heat-flux perturbation [Eq. (11b)] with $(n, k_\perp) = (4, 1)$ visualized in (m, t) coordinates. Pseudocharacteristic variable: (a) $\log |\widehat{\mathcal{W}}_1|$, (b) $\text{slog}_{10^3}(\widehat{\mathcal{W}}_2)$, (c) $\text{slog}_{10}(\widehat{\mathcal{W}}_4)$, (d) $\text{slog}_{10^3}(\widehat{\mathcal{W}}_3)$; Kovásznay modes: (e) pressure $\text{slog}_{10^3}(\widehat{p})$, (f) entropy $\text{slog}_{10^3}(\widehat{s})$, and (g) potential vorticity $\text{slog}_{10^2}(\widehat{\omega}_\perp/\rho)$ [28]. Trajectories of the mean position of the ablation front ($\times$), CJ point ($\ast$), and shock front ($\square$). Dash lines represent characteristic trajectories: $\mathcal{C}_1$, $\mathcal{C}_2$, $\mathcal{C}_4$, and $\mathcal{C}_3$ characteristics are constant m lines. The first $\mathcal{C}_1$ and $\mathcal{C}_2$ characteristics originate from the pulse half-height [Eq. (11a)], while the subsequent characteristics originate from the interactions of significant perturbation signals with the shock front, the external surface, and the ablation front.

fraction is trapped into the ablation layer as a perturbation $\widehat{\mathcal{W}}_2$. Such a trapping phenomenon is the consequence of the sign reversal of $q = \lambda_2 + \rho u'$. In the conduction region close to the ablation front $q > 0$, therefore, no perturbation $\widehat{\mathcal{W}}_2$ originating from the ablation layer can propagate in the conduction region. On the opposite $q < 0$ in the postshock region. So no perturbation $\widehat{\mathcal{W}}_2$ originating from the ablation layer can propagate into the postshock region. As a consequence perturbations $\widehat{\mathcal{W}}_2$ remain stuck in the ablation layer.

A comparison with a decomposition of perturbations into Kovásznay modes—namely perturbations of pressure, $\widehat{p}$, of

entropy, $\widehat{s}$, and of potential transverse vorticity, $\widehat{\omega}_\perp/\rho$, where

$$\widehat{\omega}_\perp = \frac{\rho}{i\,k_\perp}\,\partial_m\widehat{d}_\perp - i\,k_\perp\widehat{v},$$

highlights the additional information provided by the present pseudocharacteristic variables $(\widehat{\mathcal{W}}_i)$ [28]. The decomposition into Kovásznay modes has already been applied to ablation flows and has been found to be relevant in the postshock region [21]. Indeed, entropy perturbations [Fig. 4(f)] correspond to $\mathcal{W}_2$ and pressure perturbations [Fig. 4(e)] appear to result from the superposition of both forward and backward
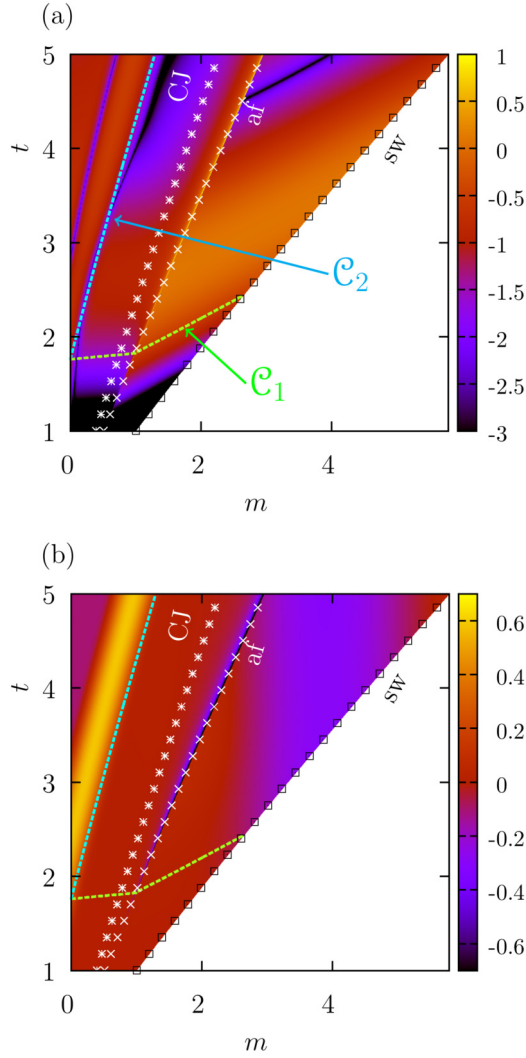
(a)

(b)

FIG. 5. Response of Eq. (4) to a pressure perturbation [Eq. (11a)] with $(n, k_\perp) = (4, 0)$ projected on (a) $\log |\widehat{\mathcal{W}}_1|$ and (b) $\mathrm{slog}_1(\widehat{\mathcal{W}}_2)$. Conventions similar to Fig. 4. The dash lines represent $\mathcal{C}_1$ and $\mathcal{C}_2$ characteristics originating from the pulse half maximum [Eq. (11b)].

FIG. 6. Schematic representation of perturbation propagation in the (m, t) plane originating from a heat-flux perturbation at the external surface. Perturbation trajectories are sketched as colored lines: $\mathcal{C}_1$ (green, densely dotted), $\mathcal{C}_2$ (cyan, loosely dashed), and $\mathcal{C}_4$ (red, solid). Arrows indicate the propagation direction. The thickness and number of arrows render the intensity of the corresponding signal. Trajectories of CJ point, ablation front ("af"), and shock front ("sf") also indicated.

acoustic waves: namely $\widehat{\mathcal{W}}_1$ and $\widehat{\mathcal{W}}_4$ in the postshock region [Figs. 4(a) and 4(c)]. However, the propagation direction of acoustic waves cannot be determined from the pressure signal while this information is available from the pseudocharacteristic variables with the distinction between forward and backward waves. No conclusion could have been deduced from Kovásznay modes into the conduction region. In the conduction region, the pseudocharacteristic variables $\widehat{\mathcal{W}}_1$, $\widehat{\mathcal{W}}_2$, $\widehat{\mathcal{W}}_4$ follow initially the trajectories of the characteristics $\mathcal{C}_1$, $\mathcal{C}_2$, and $\mathcal{C}_4$, respectively, whereas the Kovásznay mode characteristic quantities $\widehat{p}$ and $\widehat{s}$ do not present equivalent features. Indeed, pressure perturbations $\widehat{p}$ [Fig. 4(e)] coincide mainly with contributions from both pseudocharacteristic variables $\widehat{\mathcal{W}}_2$ and $\widehat{\mathcal{W}}_4$ [Figs. 4(b) and 4(c)], which correspond here to quasi-isothermal acoustic waves (Table II). Furthermore, entropy perturbations $\widehat{s}$ [Fig. 4(f)], in addition to following also the acoustic wave characteristics, propagate along the characteristics $\mathcal{C}_1$ of the supersonic heat-conductivity waves. Consequently the variables $\widehat{\mathcal{W}}_1$, $\widehat{\mathcal{W}}_2$, and $\widehat{\mathcal{W}}_4$ are more
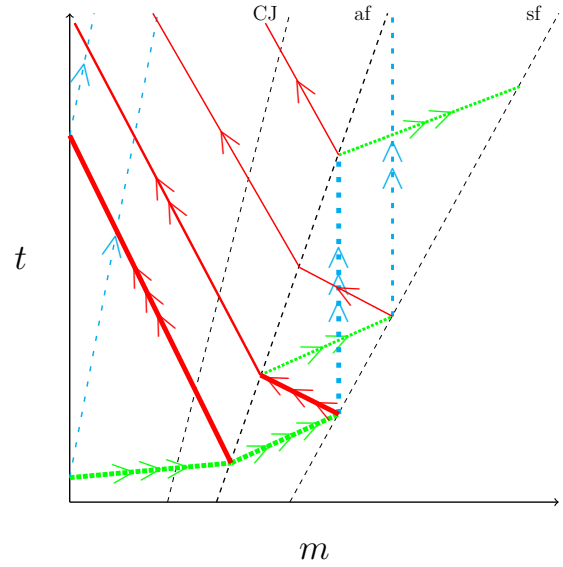
appropriate for describing perturbation evolution in the conduction region than the Kovásznay mode characteristic quantities $\widehat{p}$ and $\widehat{s}$.

Heat conductivity waves $\widehat{\mathcal{W}}_1$ in the conduction region constitute a moving source of transverse divergence for the transverse expansion perturbation $\widehat{d}_\perp$ [Fig. 4(d)]. Transverse expansion perturbations are then conveyed with the fluid (constant m coordinate) but are modified by each acoustic wave crossing the conduction region. By contrast, potential vorticity $\widehat{\omega}_\perp / \rho$ [Fig. 4(g)] presents clear constant m characteristics in both the conduction and postshock regions. Therefore, potential vorticity constitutes a better characteristic quantity for transverse perturbations than transverse expansion perturbation. The evolution equation for potential vorticity is given by [21]

$$\partial_t \left(\frac{\widehat{\omega}_\perp}{\rho} \right) = i \frac{k_\perp}{\rho^2} (\widehat{\rho} \partial_m p - \widehat{p} \partial_m \rho). \tag{12}$$

Potential vorticity is mostly created at the first interaction of the heat conductivity wave with the ablation layer (Fig. 7), where base flow density and pressure gradients are the largest. Pseudocharacteristic variables $\widehat{\mathcal{W}}_1$, $\widehat{\mathcal{W}}_2$, $\widehat{\mathcal{W}}_4$ and potential vorticity $\widehat{\omega}_\perp / \rho$ are the favored quantities for analyzing the evolution of perturbations in an ablation flow. In particular, the above analysis brings to light the pseudocharacteristic variable $\widehat{\mathcal{W}}_1$ as being the quantity of choice for identifying the propagation of perturbations from the external surface up to the ablation layer in an ablation flow with a supersonic expansion. Implications of this supersonic forward propagation of perturbations are discussed in Sec. V.
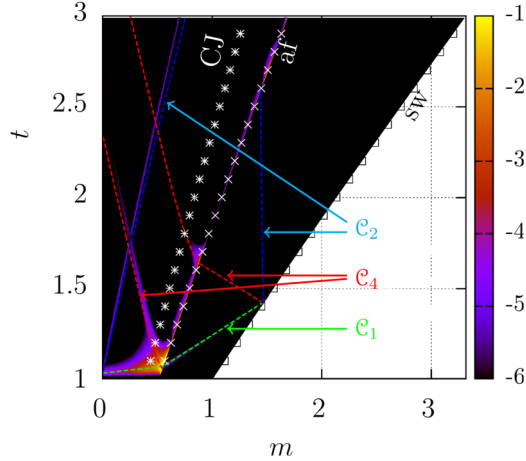
FIG. 7. Baroclinic term [Eq. (12)] in logscale for an external heat-flux perturbation $(n, k_\perp) = (4, 1)$. Dash lines represent characteristic trajectories as in Fig. 4.

A. Transmission of perturbations from the external surface to the ablation front

According to the standard modeling of radiation-driven ablation which assumes an isothermal expansion, isothermal acoustics and heat diffusion are the sole possible mechanisms for perturbation transmission from the flow external surface to the ablation front. In the present section we examine whether or not heat-conductivity waves may contribute to this transmission, in what proportion relative to heat diffusion, and under which conditions. We do so by analyzing responses to external pressure and heat-flux perturbations, for various transverse wave numbers $k_\perp$ and longitudinal characteristic lengths $\lambda_x = n\, l_{\text{cond}}$.

First order deformations of the external surface, the ablation front and the shock front, are shown on Fig. 8 in the case $(n, k_\perp) = (4, 0)$ after normalization to unity according to an energy flux measure

$$E(\widehat{\mathbf{U}}_{\text{es}}) = \left(\int_{t_0}^{T} \widehat{\varphi}_{\text{es}}^2 + (v\widehat{p}_{\text{es}})^2 dt \right)^{\frac{1}{2}}. \quad (13)$$

The case $k_\perp = 0$ is interpreted as the limit of very large transverse wavelength compared to the conduction region. For a given external perturbation energy [Eq. (13)], a pressure perturbation induces a higher shift than a heat-flux perturbation. In both cases the external surface is immediately shifted: inwardly in the case of a pressure perturbation because of a compression at the external surface and outwardly in the case of a heat-flux perturbation because of the material expansion due to a temperature increment. The first motion of the ablation front (Fig. 8) corresponds to the arrival of the forerunning heat-conductivity wave identified on Figs. 4 and 5. The same effect is observed at the shock front with a delay corresponding to the acoustic crossing time of the postshock region. The following motions of the external surface, ablation, and shock front correspond to the interactions of the traveling waves observed on Figs. 4 and 5 with the above mentioned interfaces. Consistent with the existing results, a purely longitudinal perturbation ($k_\perp = 0$) induces a permanent shift of
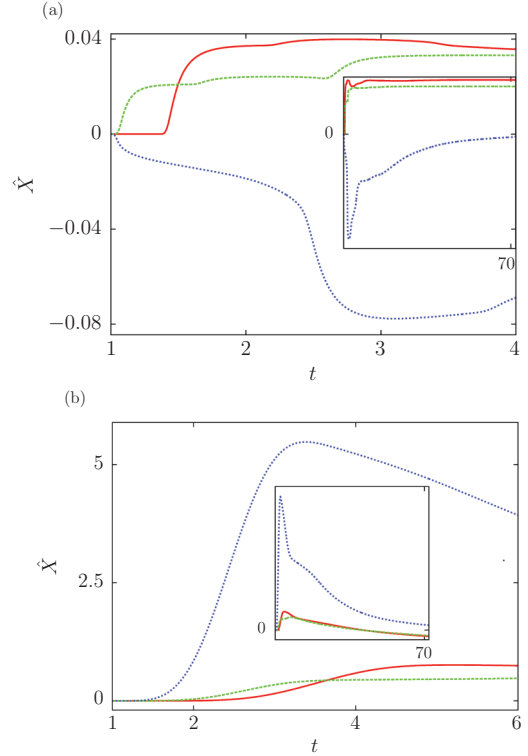

FIG. 8. Deformations of the shock front $\widehat{X}_{\text{sf}}$ (red, solid), the ablation front $\widehat{X}_{\text{af}}$ (green, dashed), and the external surface $\widehat{X}_{\text{es}}$ (blue, dotted) for (a) a longitudinal heat-flux and (b) pressure perturbation $(n, k_\perp) = (4, 0)$, normalized to unity [Eq. (13)]. These deformations are first order perturbations of mean positions appearing on Fig. 4. The insets illustrate long time behaviors.

the ablation layer and shock front [10,20,26]. To measure the efficiency of perturbation transmission from the external surface to the ablation layer, we consider the ratio

$$r = \frac{\max_t \{\|\widehat{\mathbf{U}}\|_2|_{\text{af}}\}}{\max_t \{\|\widehat{\mathbf{U}}\|_2|_{\text{es}}\}}, \quad \text{where } \|\widehat{\mathbf{U}}\|_2 = \sqrt{\sum_{i=1}^{4} \widehat{\mathbf{U}}_i^2}. \quad (14)$$

This ratio measures the amplification of a signal between the external surface and the ablation layer. The amplification is greater for an external heat-flux perturbation than for a pressure perturbation (Table III). This fact corroborates the higher ablation front deformation, relative to the external surface deformation, in the case of an external heat-flux perturbation than in the case of an external pressure perturbation (Fig. 8). This is again a consequence of the ability of heat-conductivity wave perturbations to trace back the expansion flow, unlike acoustic perturbations.

TABLE III. Amplification factor r [Eq. (14)] between the external surface and the ablation front, for a heat-flux and external pressure perturbation [Eq. (11a)] with $(n, k_\perp) = (4, 0)$.

$\widehat{p}_{\text{es}}$	$\widehat{\varphi}_{\text{es}}$
$2,29 \times 10^3$	$8,41 \times 10^3$

TABLE IV. Amplification factor r [Eq. (14)] between the external surface and the ablation front for an external heat-flux perturbation [Eq. (11a)] at various n and $k_\perp$.

		$k_\perp$		
		0	1	10
n	4	8.41×10^3	3.68×10^3	1.10×10^{-1}
	0,5	2.9×10^3	1.10×10^3	

The effects of diffusion on a heat-flux perturbation are investigated with (i) a shorter longitudinal characteristic length, $n = 0.5$ [Eq. (11)], and (ii) a transverse wave number increased to 1 and 10. The efficiency of the transmission is reduced but still persists for a longitudinal characteristic length being half of the conduction region size, $n = 0.5$ (Table IV). In particular, the ablation front deformation is lowered (Fig. 9, red), but its behavior is qualitatively similar to the case $n = 4$ (Fig. 9, blue). Therefore, a longitudinal characteristic length being a fraction of the conduction region size does not inhibit the heat conductivity wave that provokes the first shift of the ablation layer and still allows information to be transmitted to the ablation layer from the external surface. Damping effects of transverse diffusion are much stronger than longitudinal diffusion (Table IV), as a transverse wavelength of five times the conduction region ($k_\perp = 1$) implies a damping similar to a longitudinal characteristic length of half of the conduction region. Perturbations are efficiently transmitted to the ablation front only for transverse wavelengths that are over several times the conduction region size. Transverse diffusion also implies a transient relaxation after each growth phase (Fig. 9, pink and green). For transverse wavelengths being a fraction of the conduction region or smaller ($k_\perp \geqslant 10$), the transmission to the ablation layer and the ablation front deformation is negligible. At larger times, and $k_\perp > 0$, we recover the well known shock front oscillations [7,13,16,17,20,26].

B. Dominant mechanisms

We have observed earlier (Sec. IV) that perturbations qualitatively follow characteristics' trajectories from Eq. (9) in the conduction and the postshock region. In the present section
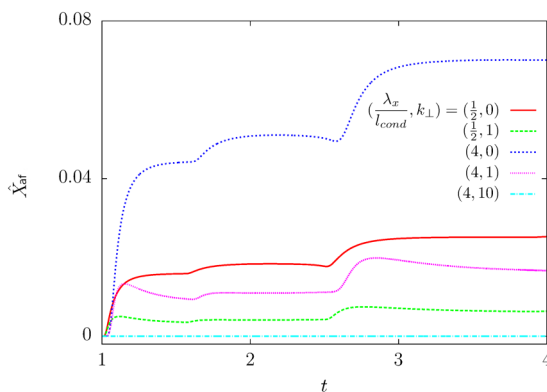

FIG. 9. Deformation of the ablation front $\widehat{X}_{af}$ at early times for different longitudinal characteristic $\lambda_x/l_{cond} = \{1/2, 4\}$ and transverse wave numbers $k_\perp = \{0, 1, 10\}$.
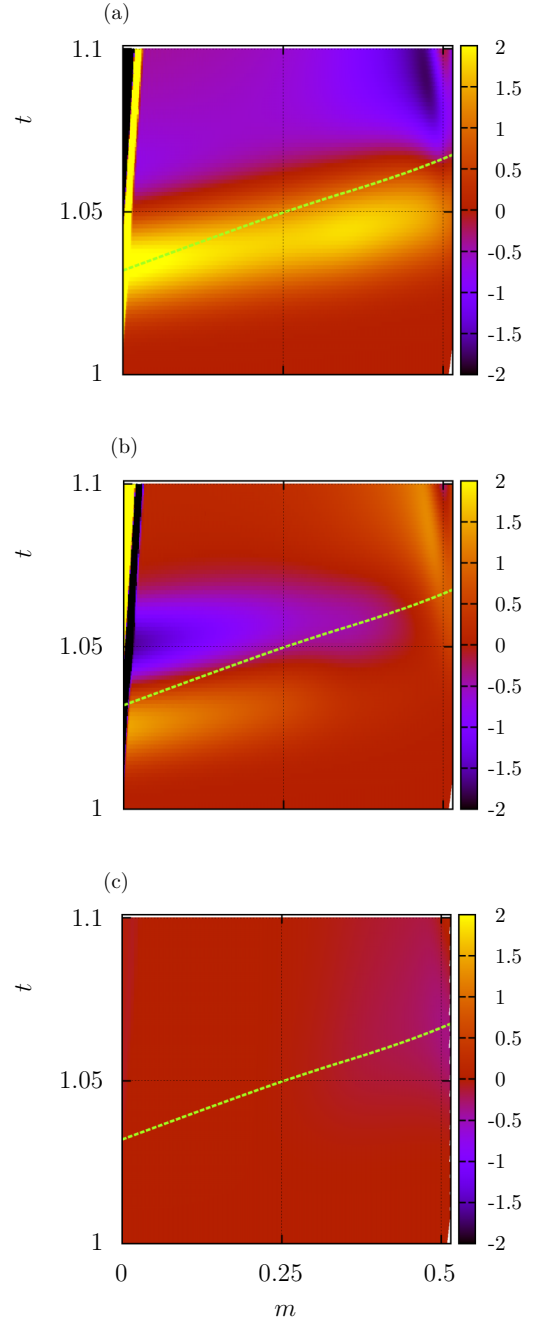

FIG. 10. Contribution from (a) advection, (b) diffusion, and (c) remaining terms from Eq. (10a) to the variation rate of $\widehat{\mathcal{W}}_1$ $(n, k_\perp) = (4, 1)$. The dash line represents a $\mathcal{C}_1$ characteristic trajectory originating from the top of the heat-flux pulse [Eq. (5)].

we carry out a quantitative analysis to discriminate between the main propagation mechanisms: advection or diffusion. Recalling Eq. (10a), the contributions from diffusion, advection, and amplification terms, to any of the pseudocharacteristic component variation rate, can be compared at any given flow location and time. The contributions to $\widehat{\mathcal{W}}_1$ in the conduction region for a purely longitudinal heat-flux perturbation [Eq. (11a)] are shown on Fig. 10. Diffusion intensity rapidly decays as the signal propagates inside the conduction region. Contributions from amplification terms and noncharacteristic
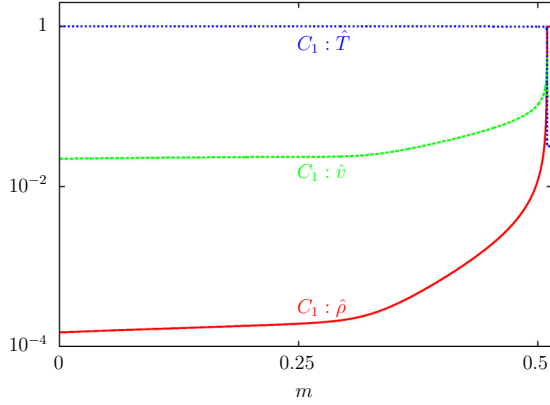
FIG. 11. Contributions of primitive variables $(\widehat{\rho}, \widehat{v}_x, \widehat{T})$ in a unit heat-conductivity wave quantity $(\widehat{\mathcal{W}}_1)$ conserved along $\mathcal{C}_1$ in Eq. (9), with no contribution from transverse velocity. Zoom in the conduction region.

terms [$\Delta\widehat{\mathcal{W}}$ in Eq. (10a)] are negligible even in the ablation layer neighborhood. Therefore, the dominant mechanism enabling heat-conductivity wave perturbations to cross the CJ point is advection, and not diffusion. The existence of supersonic linear heat-conductivity waves is quantitatively confirmed although diffusion exists in this region. This is a direct consequence of base flow stratification in the conduction region. This advection mechanism is able to transmit any hydrodynamic perturbation taking place at the external surface to the ablation layer along a $\mathcal{C}_1$ characteristic, through the CJ point, to the ablation layer.

The quantity $\widehat{\mathcal{W}}_1$ is conserved, in first approximation, along $\mathcal{C}_1$. The composition of a $\mathcal{C}_1$ wave varies across the conduction region but temperature is dominating (Fig. 11). Although the contribution of density in the conserved $\widehat{\mathcal{W}}_1$ wave increases as the wave comes up to the ablation layer, its contribution becomes significant at some location where advection no longer dominates (Fig. 3). Therefore, the heat-conductivity wave reaching the ablation layer is mostly composed of a temperature perturbation, as observed on Fig. 3(c).

In the three following sections we broaden this analysis to find out which mechanism dominates depending on the flow location and characteristic length, keeping only dominant terms from Eq. (10a). We are interested in orders of magnitude of the various quantities and not in their actual values.

1. Dominance of advection

Advection mechanism dominates where (i) diffusion terms, (ii) amplification terms, and (iii) first order coupling terms are sufficiently low. The latter is verified in the conduction region and the postshock region, whatever the wavelength of perturbations. More generally the case of the postshock region has been extensively studied in [21]. As heat flux is quasinonexistent and the stratification is moderate in this region, advection is the leading mechanism for perturbations over a wide range of wavelengths.

We have seen previously that pseudocharacteristic variables behave close to linear waves in the conduction region for $(1/2 \leqslant n \leqslant 4, 0 \leqslant k_\perp \leqslant 1)$. Let k_i denote the wave number of a linear wave approximating the pseudocharac-

teristic wave $\widehat{\mathcal{W}}_i$ and ω be the pulsation common to such waves for $i = 1, 2, 4$. The magnitude of spatial derivatives is approximated by

$$\left|\partial_m^p \widehat{\mathcal{W}}_i\right| \approx k_i^p |\widehat{\mathcal{W}}_i|, \quad \text{for } p = 0, 1, 2, \quad i = 1, 2, 4. \quad (15)$$

The pulsation ω is driven by the number of wavelengths n in the conduction region [Eq. (11)]. In the case of a heat-flux perturbation

$$\omega = k_1 \lambda_1 = \frac{2\pi \lambda_1}{n \, \rho \, l_{\text{cond}}}, \quad k_i = \omega/\lambda_i \text{ for } i = 2, 4.$$

For a given n, $k_{2,4} \gg k_1$ as $\lambda_1 \gg \lambda_{2,4}$, meaning that for a given pulsation quasi-isothermal acoustic waves are sharper than heat-conductivity waves. As a consequence second order derivatives of quasi-isothermal acoustic waves are greatly enhanced compared to those of heat-conductivity waves. Dominating contributions of each pseudocharacteristic variable $\widehat{\mathcal{W}}_j$ to each variation rate $\partial_t \widehat{\mathcal{W}}_i$ through second order derivatives (diff), first order derivatives (adv), and amplification terms (amp) are shown in Fig. 12. These contributions depend on powers of the wave number, k_i^p [Eq. (15)], and approximate values of $\mathcal{A}_{ij}$, Λ_{ii}, and $\mathcal{C}_{ij}$ in the conduction region.

For $1 \lesssim n \lesssim 10$ advection dominates diffusion for heat-conductivity and acoustic waves [Fig. 12(a)]. Simplified expressions for the respective variation rates are written as

$$\partial_t \widehat{\mathcal{W}}_1 + \lambda_1 \partial_m \widehat{\mathcal{W}}_1 + \sum_{i=2,4} \mathcal{A}_{1i} \partial_{m^2}^2 \widehat{\mathcal{W}}_i = 0,$$

$$\partial_t \widehat{\mathcal{W}}_2 + \lambda_2 \partial_m \widehat{\mathcal{W}}_2 = 0,$$

$$\partial_t \widehat{\mathcal{W}}_4 + \lambda_4 \partial_m \widehat{\mathcal{W}}_4 = 0.$$

One first notes that terms Δ_0 [Eq. (10a)], accounting for characteristic basis dependence on base-flow spatial derivatives, are negligible regarding advection and diffusion terms, meaning that the local approximation of Ref. [25] is valid in this region and for this wavelength range. In the scenario of an external heat-flux perturbation from an initially unperturbed state, a wave $\widehat{\mathcal{W}}_1$ will be advected along a $\mathcal{C}_1$ characteristic autonomously since the term $\sum_{i=2,4} \mathcal{A}_{1i} \partial_{m^2}^2 \widehat{\mathcal{W}}_i$ vanishes. This scenario corresponds to the perturbation history displayed in Figs. 2, 4, and 10. However, as an external heat-flux perturbation perturbs the external surface, a small acoustic perturbation is also emitted [Fig. 9(b)], which produces a feedback through first and second derivative coupling terms. This coupling explains the very intense tracks following a $\mathcal{C}_2$ characteristic on Figs. 10(a) and 10(b). An external pressure perturbation will be advected along a $\mathcal{C}_2$ characteristic as observed on Fig. 5(b). This advected acoustic signal will act as a source moving at velocity λ_2 on the heat-conductivity wave $(\widehat{\mathcal{W}}_1)$ through second order coupling terms [Fig. 5(a)]. This seeded heat-conductivity wave perturbation will be advected to the ablation front along a $\mathcal{C}_1$ characteristic. Therefore, any acoustic perturbation at the external surface may in principle reach the ablation front by a second derivative coupling from acoustic to heat-conductivity waves.

2. Dominance of diffusion

As stated in the preceding section, heat flux is quasinonexistent in the postshock region, so diffusion acts only for very
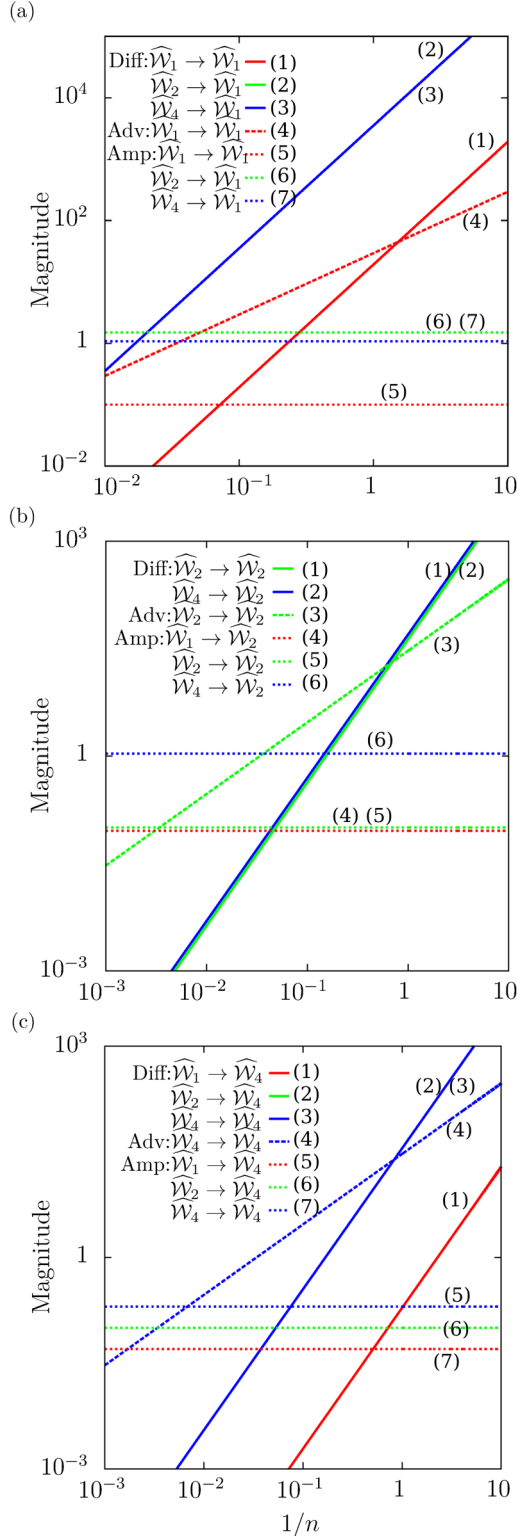
(a)

(b)

(c)

FIG. 12. Dominating terms in Eq. (10a) for (a) $\widehat{\mathcal{W}}_i \rightarrow \widehat{\mathcal{W}}_1$, (b) $\widehat{\mathcal{W}}_i \rightarrow \widehat{\mathcal{W}}_2$, and (c) $\widehat{\mathcal{W}}_i \rightarrow \widehat{\mathcal{W}}_4$, for $1/n$ [Eq. (11)] ranging from 10^{-3} to 10 and $m = 0.25$. Contribution from second order derivatives $\mathcal{A}_{ij}\partial_m^2\widehat{\mathcal{W}}_j$ (solid), first order derivatives $\mathbf{\Lambda}_{ii}\partial_m\widehat{\mathcal{W}}_i$ (dashed), and amplification terms $(\mathbb{C}_{ij} + \Delta_{ij})\widehat{\mathcal{W}}_j$ (dotted).

short wavelengths. In the ablation layer amplification terms dominate diffusion. For short wavelengths $n \leqslant 0.1$ second order derivative terms, including diffusion, dominate in the

conduction region (Fig. 12) and variation rates may be approximated by

$$\partial_t \widehat{\mathcal{W}}_1 + \mathcal{A}_{11}\partial_{m^2}^2 \widehat{\mathcal{W}}_1 + \sum_{i=2,4} \mathcal{A}_{1i}\partial_{m^2}^2 \widehat{\mathcal{W}}_i = 0,$$

$$\partial_t \widehat{\mathcal{W}}_2 + \mathcal{A}_{22}\partial_{m^2}^2 \widehat{\mathcal{W}}_2 + \mathcal{A}_{24}\partial_{m^2}^2 \widehat{\mathcal{W}}_4 = 0,$$

$$\partial_t \widehat{\mathcal{W}}_4 + \mathcal{A}_{44}\partial_{m^2}^2 \widehat{\mathcal{W}}_4 + \mathcal{A}_{42}\partial_{m^2}^2 \widehat{\mathcal{W}}_2 = 0. \qquad (16)$$

Heat conductivity waves evolve through diffusion and second derivative couplings with forward and backward quasi-isothermal acoustic waves. The latter evolve as a coupled $\widehat{\mathcal{W}}_2$-$\widehat{\mathcal{W}}_4$ system due to diffusion; therefore, the distinction between "forward" and "backward" is no longer appropriate as propagation direction cannot be found where only diffusion acts. The coupling phenomena between heat-conductivity and acoustic waves in the case of the external heat-flux and pressure perturbations explained in the preceding section hold, as well as the validity of the local analysis.

3. Dominance of amplification terms

In the regions of low base-flow gradients, amplification terms dominate at very long wavelengths—$n \gg 10$ in the conduction region (Fig. 12). The ablation layer is a region of strong base-flow gradients. All amplification terms turn out to dominate other terms due to the stiffness of the base flow (see the ratio of characteristic lengths in Table I). In particular, it is necessary to take into account terms $\mathbf{\Delta}_0$ [Eq. (10a)] accounting for the dependence of the characteristic basis [Eq. (7)] on space derivatives, meaning that the local approximation is not valid in this region. As a consequence only amplification terms are retained from Eq. (10a) and the evolution of pseudocharacteristic variables in the ablation front is driven by

$$\partial_t \widehat{\mathcal{W}}_1 + b_{11}\widehat{\mathcal{W}}_1 + b_{14}\widehat{\mathcal{W}}_4 = 0, \quad \text{with } b_{11} < 0 \text{ and } b_{14} > 0,$$

$$\partial_t \widehat{\mathcal{W}}_2 + b_{21}\widehat{\mathcal{W}}_1 + b_{22}\widehat{\mathcal{W}}_2 + b_{24}\widehat{\mathcal{W}}_4 = 0,$$

$$\text{with} \quad b_{21} > 0 \text{ and } b_{22}, \quad b_{24} < 0,$$

$$\partial_t \widehat{\mathcal{W}}_4 + b_{41}\widehat{\mathcal{W}}_1 + b_{42}\widehat{\mathcal{W}}_2 + b_{44}\widehat{\mathcal{W}}_4 = 0, \qquad (17)$$

where $b_{ij} = \mathbb{C}_{ij} + \mathbf{\Delta}_{0_{ij}}$ [Fig. 13(c)]. As a consequence a heat-conductivity wave is strongly self-amplified in the ablation front and does not experience any sign change while crossing the ablation front, as observed on Fig. 4. The quantity $\widehat{\mathcal{W}}_2$ is also self-amplified, additionally to the trapping mechanism described in Sec. IV, due to the coefficient b_{22}. Because of the sign of b_{21}, a heat-conductivity wave eventually gives rise to a wave $\widehat{\mathcal{W}}_2$ of opposite sign when it reaches the ablation layer. A backward acoustic wave originating from the postshock region will also seed a positive reflected forward acoustic wave, consequently maintaining a system of reflected traveling waves between the ablation and shock front. This approximate analysis confirms the observations made on Figs. 4 and 5. No particular driving source term can be identified for the evolution of the quantity $\widehat{\mathcal{W}}_4$ in the ablation layer because none of them dominates and two of them experience a sign change across the ablation layer [Fig. 13(c)]. For a forward propagating perturbation coming from the conduction region
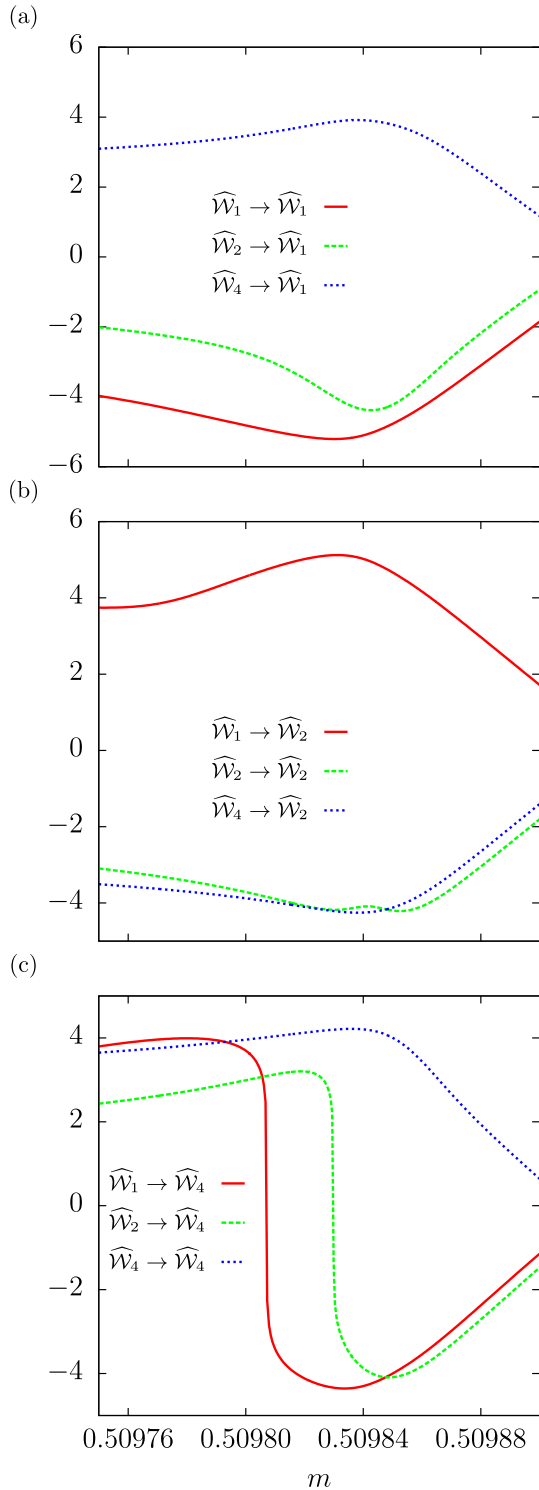
$$b_{41} \sim b_{44} \gg b_{42},$$

FIG. 13. Magnitude of dominating amplification terms in the ablation layer, (a) $\widehat{\mathcal{W}}_i \to \widehat{\mathcal{W}}_1$, (b) $\widehat{\mathcal{W}}_i \to \widehat{\mathcal{W}}_2$, and (c) $\widehat{\mathcal{W}}_i \to \widehat{\mathcal{W}}_4$.

so a heat-conductivity wave interacting with the ablation front free from perturbation will seed a backward acoustic wave in the conduction region, as observed on Figs. 4 and 5.

V. DISCUSSION

The present analysis of linear perturbation propagation in an ablation wave has confirmed the existence of heat-conductivity linear waves in the flow conduction region. This existence is the direct consequence of temperature and density stratification in the conduction region and therefore cannot be obtained from the standard modeling of radiation-driven ablation flows which assumes an isothermal expansion region (e.g., Refs. [1,18]). Such waves correspond to the propagation of fluctuations of heat-flux perturbations (Ref. [25], Sec. 4.2). They are presently found to be an efficient transmission mechanism for perturbations of longitudinal characteristic lengths of the order of—or larger than—the conduction region size and of transverse wavelengths being several times this size. Under these conditions, this transmission by advection prevails over heat diffusion and is, by essence, free of any damping.

Due to their high propagation velocity, heat-conductivity waves propagate from the external surface to the ablation layer in a fraction of the acoustic crossing time of the postshock region, which is itself a fraction of the shock transit phase duration. Therefore, heat-conductivity waves may occur for perturbations of the external heat flux and/or pressure over time scales shorter to much shorter than that of the shock transit phase.

Because of second order spatial derivative couplings near the external surface between forward-propagating acoustic and heat-conductivity waves, any hydrodynamic perturbation at the external surface may be partly advected through the conduction region, beyond a potential Chapman-Jouguet point, up to the ablation front. Hence even fluctuations of the fluid velocity or pressure at the flow external surface may have an impact on the rest of the ablation flow, including the ablation and shock fronts, in the case of a supersonic expansion flow. This transmission process may be effective at any time of an ablation flow provided that the temperature stratification in the conduction region is sufficiently high. This refined analysis of perturbation propagation furnishes a deeper understanding of perturbation feedthrough in ablation flows due to nonlinear heat conduction.

The present results of linear perturbation propagation have been obtained for a particular self-similar ablation wave representative, through its gross hydrodynamic features, of the shock transit phase of an ICF implosion. The present base-flow self-similarity implies that the radiation heat flux as well as the exerted pressure at the flow external surface follow increasing time-power laws [Eq. (3)]. These specific behaviors are far from being observed in radiation hydrodynamic simulations of the shock transit phase of an ICF pellet during the foot of the radiation drive. However, simulated flow profiles obtained for an actual ICF target design and radiation drive (Figs. 1 and 5 in [29]), in the radiation heat-conduction approximation, do not qualitatively differ, for the conduction region, from those of a suitably chosen self-similar ablation wave (Fig. 2 in [25]). Since the properties of heat-conductivity waves are determined by the base-flow temperature and density stratifications in this region, we may expect to also observe forward-propagation of perturbations by supersonic heat-conductivity waves in this particular non-self-similar ICF flow. This claim is based on the fact that heat-conductivity waves with supersonic characteristic speeds have been found to occur in self-similar ablation flows presenting very different stratifications of their conduction regions [25].

The presence of such waves thus appears to be related to the high values of the heat-conduction flux in the flow conduction region rather than to the details of the temperature and density stratifications in this region. In that respect, heat-conductivity waves are expected to be present in ablation flows driven by incident heat-flux laws less specific than the time-power laws of Eq. (3). Of course, the velocities and prevailing of these waves depending on the local features of the base flow, a quantitative evaluation of the role played by such waves would require applying the present analysis in pseudocharacteristic variables to the ablation flow under study. Since this analysis is independent of any self-similarity assumption, there is no theoretical obstacle to do so, only the practical complication of dealing with an arbitrary time evolution of the base-flow variables.

Heat-conductivity waves are not restricted to radiation conduction and may occur for other types of nonlinear heat conduction, e.g., electron heat conduction. In this latter case, the linear wave analysis proposed in the present work could be applicable to the entire extent of a laser-driven ablative wave, i.e., including the plasma corona expansion, and should be especially relevant in the region between the surface of laser energy deposition and the leading shock front. Such an analysis could even be elaborated and carried out for self-similar solutions of a two-temperature modeling of laser-driven ablation plasmas [30]. In the case of radiation-driven ablation of an ICF pellet, the approximation of radiation heat conduction is justified only for the optically thick part of the ablated material. Therefore, the present analysis is relevant to a portion of the ablation wave that starts at some distance downstream to the ablation layer and extends up to the forerunning shock front. Perturbations, with large transverse wavelengths, of the incoming radiation intensity at the ablator external surface are efficiently transmitted across the optically thin region of the expanding flow, resulting in perturbations of the radiation heat flux at the edge of the conduction region. Since such heat-flux perturbations correspond for a part to the characteristic quantity advected by supersonic heat-conductivity waves, we can still expect to observe the propagation, in addition to the diffusion, of such waves deeper into the conduction region. Obtaining a quantitative assessment of such a process in order to go beyond this conjecture, would require at first to extend the present analysis to the modeling of nonequilibrium radiation diffusion, a task that we leave for future works.

VI. CONCLUSION

The present work provides a numerical investigation of linear perturbations of a realistic self-similar ablation wave in slab symmetry representative of the shock transit phase of an ICF pellet implosion. The perturbation configuration that is treated differs from those of illumination asymmetries and ablative Richtmyer-Meshkov instability since we focus on the setup of perturbations in an already existing and unperturbed ablation flow, under the excitation of heat-flux or pressure perturbations at the flow external surface. The physics of ablation is modeled by the equations of gas dynamics with a nonlinear heat conduction as an approximation for radiation transport. Perturbations of flow variables are three-dimensional without any self-similarity assumption and are computed together with external surface and shock front linear deformations. Linear perturbations of the ablation layer position are provided.

Perturbations are found to behave close to linear waves in the conduction region and the postshock region. The main result is the observation of supersonic heat-conductivity waves propagating forward through the supersonic expansion flow, as predicted by Clarisse *et al.* [25], as a consequence of base flow stratification in the conduction region. This result is allowed by the choice of a modeling derived from first principles and without supplemental simplifying assumptions and could not, for example, have been obtained with the assumptions of an isothermal expansion of the flow conduction region [1,18]. As a consequence, any hydrodynamic perturbation at the external surface may be advected through the conduction region, beyond a potential Chapman-Jouguet point, up to the ablation front. Although heat diffusion is effective, linear perturbation propagation by supersonic heat-conductivity waves is found, for transverse wavelengths exceeding the size of the conduction region, to be dominant (to remain significant) for longitudinal characteristic lengths above (down to a fraction of) this size. Hence within the framework of inviscid compressible fluid dynamics with nonlinear heat conduction, diffusion of linear perturbations in the conduction region of an ablation wave should not be considered without its interplay with this supersonic advection mechanism. Accounted for in the hydrodynamic equations of ICF simulation codes treating radiation or electron heat diffusion, this mechanism, if scrutinized in simulation results, will help in getting a better qualitative and quantitative understanding of perturbation dynamics and feedthrough in ablation flows. Thus more accurate pictures of ablation flow sensitivities to external perturbations could be obtained, opening the way for investigating this mechanism as a possible means of partial control of hydrodynamic perturbations in ICF implosions. Another aspect of heat-conductivity waves is their ability to propagate density perturbations at supersonic speeds, a feature which is critical in the radiative heat transport instability [31]. However, no indication of instability has been observed in the present ablation flow for which, along heat-conductivity waves, density fluctuations are too low compared to temperature fluctuations to be of some influence. Nevertheless, heat-conductivity waves carrying higher density fluctuations may arise in other self-similar radiative ablation flows, leaving open the possibility of observing radiative heat transport instability in such flows.

More generally, the description of the flow perturbations conducted in this paper in terms of longitudinal pseudocharacteristic waves supplemented by the transverse potential vorticity of the velocity field perturbation has been found to be most appropriate for analyzing perturbation dynamics in both the conduction region and postshock region of a one-dimensional ablation flow. This description furnishes additional propagation information over the classical fundamental—Kovásznay—modes of fluid dynamics and are more relevant for the density and temperature stratified regions of such flows. The analysis performed by such a description and the companion identification of simplified evolution equations form a methodology that is fully applicable to other ablation flows whether in the context of radiation-driven or laser-driven ablation.

[1] S. Atzeni and J. Meyer-ter-Vehn, *The Physics of Inertial Fusion* (Oxford University Press, Oxford, UK, 2004).

[2] Ya. B. Zel'dovich and Yu. P. Raizer, *Physics of Shock Waves and High-temperature Hydrodynamic Phenomena* (Academic Press, New York, 1967).

[3] J. Lindl, O. Landen, J. Edwards, E. Moses, and NIC Team, Review of the national ignition campaign 2009-2012, Phys. Plasmas **21**, 020501 (2014).

[4] R. J. Taylor, J. P. Dahlburg, A. Iwase, J. H. Gardner, D. E. Fyfe, and O. Willi, Measurement and Simulation of Laser Imprinting and Consequent Rayleigh-Taylor Growth, Phys. Rev. Lett. **76**, 1643 (1996).

[5] R. D. Richtmyer, Taylor instability in shock acceleration of compressible fluids, Commun. Pure Appl. Math. **13**, 297 (1960).

[6] E. E. Meshkov, Instability of the interface of two gases accelerated by a shock wave, Sov. Fluid Dyn. **4**, 101 (1969).

[7] V. N. Goncharov, Theory of the Ablative Richtmyer-Meshkov Instability, Phys. Rev. Lett. **82**, 2091 (1999).

[8] H. J. Kull and S. I. Anisimov, Ablative stabilization in the incompressible Rayleigh-Taylor instability, Phys. Fluids **29**, 2067 (1986).

[9] M. H. Emery, J. H. Gardner, R. H. Lehmberg, and S. P. Obenschain, Hydrodynamic target response to an induced spatial incoherence-smoothed laser beam, Phys. Fluids B **3**, 2640 (1991).

[10] R. Ishizaki and K. Nishihara, Propagation of a Rippled Shock Wave Driven by Nonuniform Laser Ablation, Phys. Rev. Lett. **78**, 1920 (1997).

[11] R. J. Taylor, A. L. Velikovich, J. P. Dahlburg, and J. H. Gardner, Saturation of Laser Imprint on Ablatively Driven Plastic Targets, Phys. Rev. Lett. **79**, 1861 (1997).

[12] A. L. Velikovich, J. P. Dahlburg, J. H. Gardner, and R. J. Taylor, Saturation of perturbation growth in ablatively driven planar laser targets, Phys. Plasmas **5**, 1491 (1998).

[13] K. Nishihara, R. Ishizaki, J. G. Wouchuk, Y. Fukuda, and Y. Shimuta, Hydrodynamic perturbation growth in start-up phase in laser implosion, Phys. Plasmas **5**, 1945 (1998).

[14] N. Metzler, A. L. Velikovich, and J. H. Gardner, Reduction of early-time perturbation growth in ablatively driven laser target using tailored density profiles, Phys. Plasmas **6**, 3283 (1999).

[15] V. N. Goncharov, S. Skupsky, T. R. Boehly, J. P. Knauer, P. McKenty, V. A. Smalyuk, R. P. Town, O. V. Gotchev, R. Betti, and D. D. Meyerhofer, A model of laser imprinting, Phys. Plasmas **7**, 2062 (2000).

[16] V. N. Goncharov, O. V. Gotchev, E. Vianello, T. R. Boehly, J. P. Knauer, P. W. McKenty, P. B. Radha, S. P. Regan, T. C. Sangster, S. Skupsky, V. A. Smalyuk, R. Betti, R. L. McCrory, D. D. Meyerhofer, and C. Cherfils-Clérouin, Early stage of implosion in inertial confinement fusion: Shock timing and perturbation evolution, Phys. Plasmas **13**, 012702 (2006).

[17] Y. Aglitskiy, A. L. Velikovich, M. Karasik, N. Metzler, S. T. Zalesak, A. J. Schmitt, L. Phillips, J. H. Gardner, V. Serlin, J. L. Weaver, and S. P. Obenschain, Basic hyrdodynamics of Richtmyer-Meshkov-type growth and oscillations in the inertial confinement fusion-relevant conditions, Philos. Trans. R. Soc. A **368**, 1739 (2010).

[18] Y. Saillard, P. Arnault, and V. Silvert, Principles of the radiative ablation modeling, Phys. Plasmas **17**, 123302 (2010).

[19] F. Abéguilé, C. Boudesocque-Dubois, J.-M. Clarisse, S. Gauthier, and Y. Saillard, Linear Perturbation Amplification in Self-similar Ablation Flows of Inertial Confinement Fusion, Phys. Rev. Lett. **97**, 035002 (2006).

[20] J.-M. Clarisse, C. Boudesocque-Dubois, and S. Gauthier, Linear perturbation response of self-similar ablative flows relevant to inertial confinement fusion, J. Fluid Mech. **609**, 1 (2008).

[21] V. Lombard, S. Gauthier, J.-M. Clarisse, and C. Boudesocque-Dubois, Kovásznay modes in stability of self-similar ablation flows of ICF, Europhys. Lett. **84**, 25001 (2008).

[22] R. Marshak, Effect of radiation on shock wave behavior, Phys. Fluids **1**, 24 (1958).

[23] J. Sanz, A. R. Piriz, and F. G. Tomasel, Self-similar model for tamped ablation driven by thermal radiation, Phys. Fluids B **4**, 683 (1992).

[24] C. Boudesocque-Dubois, S. Gauthier, and J.-M. Clarisse, Self-similar solutions of unsteady ablation flows in inertial confinement fusion, J. Fluid Mech. **603**, 151 (2008).

[25] J.-M. Clarisse, J.-L. Pfister, S. Gauthier, and C. Boudesocque-Dubois, A hydrodynamic analysis of self-similar radiative ablation flows, J. Fluid Mech. **848**, 219 (2018).

[26] J.-M. Clarisse, S. Gauthier, L. Dastugue, A. Vallet, and N. Schneider, Transient effects in unstable ablation fronts and mixing layers in HEDP, Phys. Scr. **91**, 074005 (2016).

[27] C. Boudesocque-Dubois, V. Lombard, S. Gauthier, and J.-M. Clarisse, An adaptive multidomain Chebyshev method for nonlinear eigenvalue problems: Application to self-similar solutions of gas dynamics equations with nonlinear heat conduction, J. Comput. Phys. **235**, 723 (2013).

[28] L. S. G. Kovásznay, Turbulence in supersonic flow, J. Aeronautic. Sci. **20**, 657 (1953).

[29] Y. Saillard, Hydrodynamique de l'implosion d'une cible FCI, C. R. Acad. Sci. Paris Série IV **1**, 705 (2000).

[30] J. R. Sanmartín and A. Barrero, Self-similar motion of laser half-space plasma. I. Deflagration regime, Phys. Fluids **21**, 1957 (1978).

[31] V. Yu. Bychenkov and W. Rozmus, Radiative heat transport instability in a laser produced inhomogeneous plasma, Phys. Plasmas **22**, 082705 (2015).